

Mechanism of stimulated Hawking radiation in a laboratory Bose-Einstein condensate

Yi-Hsieh Wang^{1,2}, Ted Jacobson³, Mark Edwards^{1,4}, and Charles W. Clark^{1,2}

¹*Joint Quantum Institute, National Institute of Standards and Technology
and the University of Maryland, College Park, Maryland 20742,*

²*Chemical Physics Program, University of Maryland, College Park, Maryland 20742,*

³*Department of Physics and Maryland Center for Fundamental Physics,
University of Maryland, College Park, Maryland, 20742,*

⁴*Physics Department, Georgia Southern University, Statesboro, GA 30460*

We model a sonic black hole analog in a quasi one-dimensional Bose-Einstein condensate, using a Gross-Pitaevskii equation matching the configuration of a recent experiment by Steinhauer. The model agrees well with important features of the experimental observations, demonstrating their hydrodynamic nature. With enhanced but experimentally feasible parameters we establish by spectral analysis that a growing bow wave is generated at the inner (white hole) horizon, stimulating the emission of Hawking radiation. The black hole laser effect plays no role.

Using linear quantum field theory, Hawking predicted [1, 2] that a black hole of mass M should emit thermal radiation with temperature, $T = 62 \text{ nK } M_{\odot}/M$, where M_{\odot} is the mass of the Sun. Such low temperatures make it challenging to directly observe Hawking radiation (HR) from any known black hole. Unruh [3] proposed that sonic analogs of HR might be seen in hydrodynamic systems; Garay *et al.* [4] subsequently suggested gaseous Bose-Einstein condensates (BECs) as vehicles for analog HR. Corley and Jacobson [5] identified a “black hole laser” mechanism, which generates HR via an amplification process that takes place between black hole (BH) and white hole (WH) event horizons. This proposal stimulated much interest in laboratory realizations [6–13].

In 2014, Steinhauer [14] reported an experiment that implements a sonic analog black hole laser in a cigar-shaped BEC of ^{87}Rb . The BEC is swept by a step potential with the energy equivalent of a few nK. The sweep generates a low-density region of supersonic flow in the interior of the BEC, bounded by two subsonic flows at BH and WH event horizons (Fig. 1). Steinhauer observed exponential growth of an acoustic wave within the BEC, and correlations with density variations outside the BH, which he interpreted as evidence for lasing action of self-amplifying Hawking radiation.

Here we report simulations of the experiment of Ref. [14], using the time-dependent Gross-Pitaevskii (GP) equation and the experimental parameters. We find that the GP treatment accounts for important features of the observations using only BEC hydrodynamics, without quantum fluctuations. Further, we show that slightly modified parameters can result in a much more distinct signature, and employ this to establish quantitatively that the Hawking radiation in this experimental setting is *not* self-amplifying, but rather is stimulated monochromatically by a growing Bogoliubov-Čerenkov mode [15], also known as a zero-mode undulation [8, 16, 17], generated at the WH horizon. We find that the Bogoliubov-de Gennes linearized mode analysis is remarkably accurate, despite the strong nonlinearity of the BEC, and using it we verify this mechanism. We also establish that the Hawking temperature prediction is consistent with the

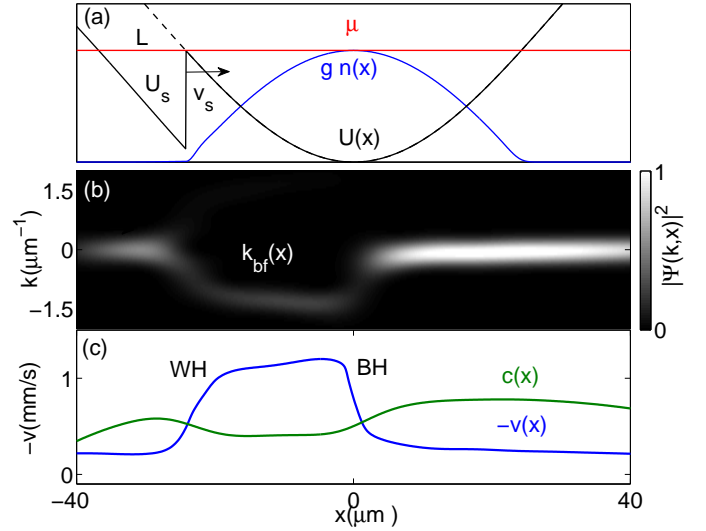


FIG. 1. (a) the potential-step structure at the start of its sweep through the BEC with number density $n(x)$, chemical potential μ and confining potential $U(x)$; (b) windowed wavevector spectrum of a BEC during the sweep, showing an accelerated flow generated by the moving step, edge at $x = 0$; the peak location is denoted by $k_{bf}(x)$; (c) the flow speed in the step frame $-v(x)$ and speed of sound $c(x)$, which are equal at the horizons, WH and BH.

relative amplitude of the Hawking radiation and partner waves, insofar as would be expected.

A study having some overlap with ours was recently reported by Tettamanti *et al.* [18]. They established the hydrodynamic character of the experimental observations, and identified the Bogoliubov-Čerenkov mode as responsible for initiating the instability, both of which are consistent with our findings. Our accounts differ, however, regarding the subsequent evolution. They report that the resulting Hawking radiation is self-amplifying, and that the growing wave pattern between the horizons results from this amplification and the interference between counter-propagating waves. We find instead that the growth is due to the increasing BEC density at the

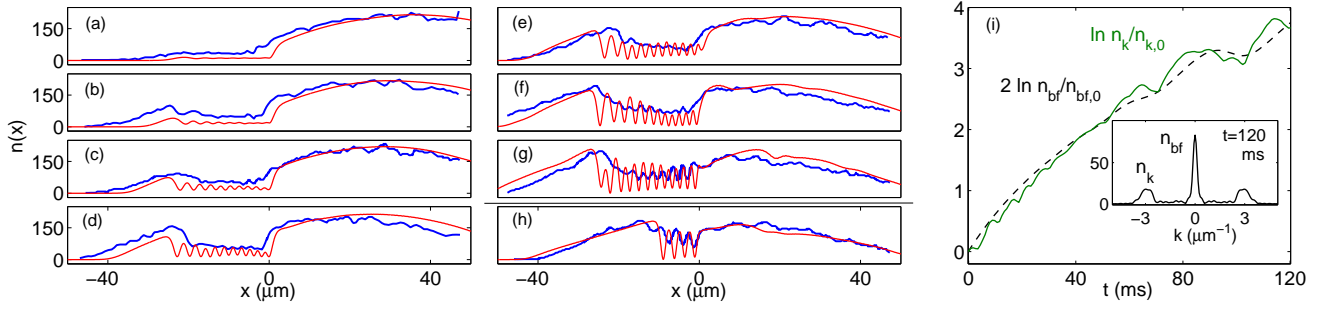


FIG. 2. (a-g) Density vs. time of a swept BEC at 20 ms intervals with step $U_s/k = 6$ nK, scaled by a common factor to match experiment, and viewed in the moving frame where $x = 0$ defines the step edge; panel (h): $U_s/k = 3$ nK at 120 ms. Blue: experiment [14]; Red: present simulation. (i) Simulated growth of the standing-wave pattern in the supersonic region for $U_s/k = 6$ nK. Dashed black: background density $n_{\text{bf}}(t)$; Green: mode growth $n_k(t)$. The growth of n_{bf} and n_k is determined from a spatial WFT of $n(x)$ at $x = -12 \mu\text{m}$. Inset shows the windowed spectrum at $t = 120$ ms.

WH horizon, and that self-amplification and interference play no role.

In the experiment of [14] a BH-WH cavity is established in a quasi-one-dimensional, laboratory BEC held by a confining potential, $U(x)$, as shown in Fig. 1(a). By sweeping a potential step of depth U_s at uniform speed v_s across the BEC, BH and WH event horizons are established. Atoms are accelerated in the direction opposite to the step motion due to the precipitous drop in the potential. This creates a supersonic flow behind the step and forms a BH horizon at the step edge, x_{BH} . The accelerated atoms gradually slow as they recede from the step, due to the rising potential. This causes the flow to become subsonic at a critical distance L behind the step, defining the WH event horizon x_{WH} , where $v(x_{\text{WH}}) = -c(x_{\text{WH}})$. Not far beyond x_{WH} the flow velocity in the lab frame drops to zero, roughly where the step-modified potential is equal to $U(x_{\text{BH}})$.

We model the experiment in [14] by solving the time-dependent one-dimensional GP equation as described in the supplementary material, using parameters matching those in the experiment. Panel (b) in Fig. 1 shows the wavevector spectrum of the GP wave function of our simulated BEC, using a windowed Fourier transform (WFT) [19] defined in the lab frame, with a Gaussian window of full width $10 \mu\text{m}$ at $1/e$, at a moment during the sweep (Fig. 2(e)). Behind the step, the accelerated component with $k \sim -1.4 \mu\text{m}^{-1}$ corresponds to supersonic flow. The blue curve in panel (c) of Fig. 1 is the flow speed in the rest frame of the step, $-v(x) = v_s - v_{\text{bf}}(x)$, where $v_{\text{bf}}(x) = \hbar k_{\text{bf}}(x)/m$ is the background flow velocity, defined by the wavevector $k_{\text{bf}}(x)$ at which the WFT of $\Psi(x)$ is peaked. The green curve is the local speed of sound $c(x) = \sqrt{g n_{\text{bf}}(x)/m}$, where $n_{\text{bf}}(x)$ is the local density of the background flow, defined here by a WFT of $n(x)$. Here m is the atomic mass and g is the mean-field interaction coefficient, as defined in the supplemental material, which also provides details of the WFT procedure.

Figs. 2(a-h) show comparisons of the simulations with experiment. Panels (a-g) show the BEC density for

$U_s = k \times 6$ nK after the launch of a sweep at 20 ms intervals, where k is the Boltzmann constant. Panel (h) corresponds to the density profile at $t = 120$ ms for $U_s = k \times 3$ nK. The coordinate origin in each panel has been displaced to coincide with x_{BH} . The density exhibits a standing-wave pattern behind the step, with amplitude growing in time. Considering that the experimental observations involve an average over any quantities that fluctuate from one run to another, the GP simulation qualitatively matches the overall evolution seen in the experiment. In particular, the growth, wavelength, and phase of the wave pattern appear consistent. (An analysis of the effect of the fluctuations on the measured density-density correlation function is beyond the scope of this paper.) It is shown in Ref. [18] that fluctuations in the location of the WH horizon over different runs can partially wash out the oscillations. Note that the presence of a definite phase in the experimental density pattern (which was collected over a large number of nearly identical runs) indicates deterministic, hydrodynamic behavior.

Ref. [14] reported exponential growth of the oscillatory density pattern in the BH-WH cavity, and suggested that it results from the black hole laser effect. Our simulations exhibit similar growth, but lead us to attribute it to a different mechanism. Panel (i) of Fig. 2 displays the growths of the background flow density n_{bf} and of a standing wave, n_k , that is defined by the peaks of the WFT of the density at $x_{\text{BH}} - 12 \mu\text{m}$, as shown in the inset. Over 120 ms the standing wave density grows by $\sim \exp(3.7)$.

Regarding the mechanism, note that the step moves toward the region of higher BEC density (see Fig. 1(a)), so both n_{bf} and n_k grow together. Panel (i) of Fig. 2 shows that n_k grows in proportion to n_{bf}^2 . This relation can be explained as resulting from the Čerenkov effect. An obstacle in a stationary supersonic flow produces an upstream, Bogoliubov-Čerenkov standing wave [15, 20], analogous to a bow wave on water [21]. It was observed in Ref. [8] that such a standing wave is generated at a

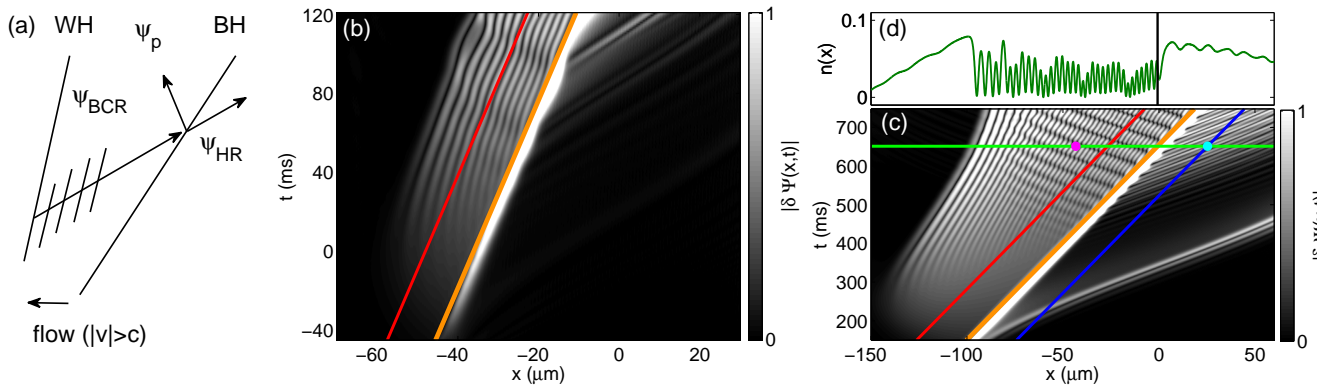


FIG. 3. BCR-stimulated pair production, viewed in the lab frame, where $x = 0$ at the center of the original trap. (a) HR (ψ_{HR}) and its partner (ψ_p) created at the BH by right-propagating BCR (ψ_{BCR}) generated at the WH as a standing wave; Panels (b-c): time evolution of $|\delta\Psi(x,t)|$, multiplied by 10 for $x > x_{BH}$, where x_{BH} is shown by the solid orange lines. (b) Experimental parameters [14] with $U_s/k = 6$ nK. (c) Enhanced regime M2 (see text). The red and blue lines indicate the paths on which the windowed frequency spectra of Fig. 4(b) are calculated. The wavevector spectrum along the green line is shown in Fig. 4(c). (d) Density $n(x)$ at $t = 650$ ms, along the green line in (c). The magenta dot and cyan dot correspond to a correlated Hawking pair, for which the thermal prediction is being tested.

WH horizon, triggered by an incident wavepacket on the stationary flow, and saturating at an amplitude determined by nonlinear effects. In our case, the subsonic component on the LHS of the WH horizon serves as an obstacle in the supersonic flow, generating a Bogoliubov-Čerenkov wave whose saturated amplitude (n_k) should be proportional to the strength of the obstacle times the density of the background flow (n_{bf}) [15, 22]. Since the “obstacle” itself has a strength proportional to the BEC density to the left of the WH horizon, which grows similarly to that on the right, the saturated wave amplitude n_k grows as n_{bf}^2 . This growth $\sim \exp(3.7)$ compares well with $\sim \exp(3.3)$ measured experimentally via the FT of the normalized density-density correlation function [14], which presumably was, in effect, a measurement of the quantity $n_k^2/n_{bf}^2 \propto n_k$.

A Bogoliubov-Čerenkov mode should have zero frequency in the frame of the WH horizon. This corresponds to a nonzero frequency in the BH horizon frame because, as can be seen in Fig. 3, the WH horizon velocity is less than the BH horizon velocity. This mode will stimulate Hawking pair emission at the latter frequency, with wavevectors determined by the Bogoliubov-de Gennes (BdG) spectrum at this frequency, since the flow is approximately stationary in the WH and BH frames; cf. Fig. 3(a). In the following we closely examine the full process, first using a spacetime representation of the evolving BEC, and then using spectral analysis. These methods allow us to verify this mechanism, to directly relate the fully nonlinear GP behavior to that of the linearized, BdG modes on the background flow, and to compare with the Hawking temperature prediction.

To resolve the Hawking radiation, we subtract the dominant, slowly varying background $\bar{\Psi}$, determined by the static trap potential, from the full GP wavefunction Ψ . With $\bar{\Psi}$ defined as the average of Ψ over a spa-

tial interval of length $2D$ around each x , the difference $\delta\Psi \equiv \Psi - \bar{\Psi}$ characterizes the part of Ψ composed roughly of wavevectors $k \gtrsim \pi/D$. We choose D to be large enough so that $\bar{\Psi} \approx 0$ between the horizons, yet small enough to capture the slow variations of the background outside the horizon. Fig. 3(b) shows a density plot of the evolution of $|\delta\Psi|$ (with $D = 5.4 \mu\text{m}$), using the parameters of Steinhauer’s experiment [14]. The portrait displays an interference pattern between the background flow and excited modes of $\delta\Psi$. The evolution of the BH horizon is indicated by the orange diagonal line. To clearly display $|\delta\Psi|$ upstream of the horizon we have multiplied it there by a factor of ten.

To enhance the signature of this process, we ran simulations over ranges of the parameters, $U(x)$, U_s , and v_s , to find regimes where the amplitudes of all relevant modes are sufficiently large, and their wavelengths sufficiently small relative to the variation of the background flow, to permit an accurate WKB description of local modes. This investigation is described in the supplementary material. Figs. 3(c-d) and 4 show results in one such regime (case M2), for which the trap potential is widened so that the BEC is twice as long as in the experiment, the step size is 3.6 nK, and the step speed of 0.2 mm/s is 0.94 times that of the experiment. The features in the M2 regime that we now highlight are also visible in the experiment, though less distinctly.

At the beginning of the evolution shown in Fig. 3(c), a shock wave is generated due to the arrival of the step at the edge of the BEC. As the condensate spills over the step, a left-moving flow develops, as indicated by the growing light gray area. When this flow reaches the WH horizon, at $t \approx 250$ ms, a wave of Bogoliubov-Čerenkov radiation (BCR) is generated because the WH horizon is moving supersonically with respect to the condensate. As in the experimental parameter regime, the BCR grows

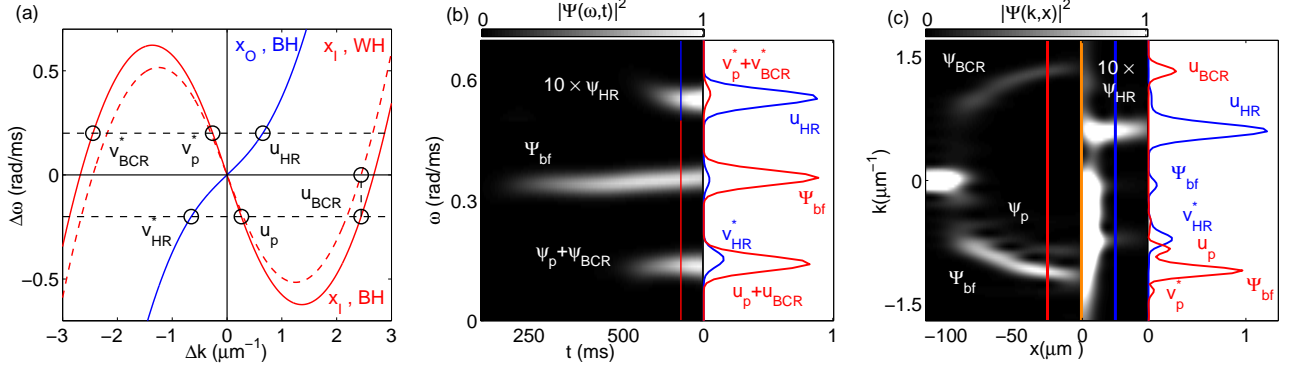


FIG. 4. Dispersion relations and WFTs of $\Psi(x, t)$ ($\delta\Psi(x, t)$ for $x > x_{\text{BH}}$) along the lines indicated in Fig. 3(c). (a) dispersion relations at x_I in the WH (dashed red) and BH (solid red) reference frames, and at x_O in the BH reference frame (solid blue), evaluated at $t = 650$ ms. $\Delta\omega$ and Δk are the frequency and wavevector relative to those of the background flow. (b) frequency spectrum along the diagonal red (x_I) and blue lines (x_O); (c) wavevector spectrum along the horizontal green line ($t = 650$ ms).

in proportion to n_{bf}^2 as a standing wave of zero frequency (with respect to that of the background flow component) in the rest frame of the WH horizon. The BCR first reaches the BH horizon at $t \approx 400$ ms, stimulating emission of Hawking radiation with the frequency of the BCR as measured in the rest frame of the BH horizon. The frequency of $|\delta\Psi|$ appears doubled outside the BH compared to that inside. This is because $\delta\Psi$ contains very little background flow component with which to interfere outside the BH, so the visible interference is between the positive and negative relative frequency parts of the HR. The left-moving partner radiation resulting from the “pair creation” forms a “V”-shape with the Hawking radiation, and makes an interference pattern with the BCR. (Were there no mode present to stimulate the pair creation, it would nevertheless occur spontaneously, as in the Hawking effect for an astrophysical black hole.)

The process just described is illustrated in Fig. 3(a). Using the BdG theory of linearized modes [22], this mechanism can be verified by comparing its spectral predictions to the numerically measured spectra. To make contact with the notion of linearized, BdG modes and their dispersion relation, we locally factor the full GP wavefunction $\Psi(x, t)$ into a homogeneous background Ψ_{bf} and the deviation ψ , so that the deviation is locally a superposition of harmonic modes of the form

$$\psi_j = (u_j e^{-i\Delta\omega_j t + i\Delta k_j x} + v_j^* e^{+i\Delta\omega_j t - i\Delta k_j x}) \times e^{-i\omega_{\text{bf}} t + i k_{\text{bf}} x}, \quad (1)$$

where $j = \text{p, HR, BCR}$. Each BdG mode is composed of two components, with opposite frequency and wavevector, $\pm(\Delta\omega_j, \Delta k_j)$, relative to those of the background flow, $(\omega_{\text{bf}}, k_{\text{bf}})$. The BdG relation is given by

$$\Delta\omega = \sqrt{(\hbar\Delta k^2/2m)^2 + c^2\Delta k^2} + v_o\Delta k, \quad (2)$$

where v_o is the velocity of the condensate with respect to the “observer” frame in which the frequency is defined. The square root term gives the frequency in the rest frame of the condensate.

The dispersion relations evaluated inside and outside the BH at $t = 650$ ms are shown in Fig. 4(a). The red and blue solid curves indicate the dispersion relation in the BH horizon frame ($v_o = v_{\text{BH}}$), at $x_I = x_{\text{BH}} - 26 \mu\text{m}$ and $x_O = x_{\text{BH}} + 26 \mu\text{m}$, respectively. The dashed red curve also indicates the dispersion relation at x_I , but referred to the WH horizon frame ($v_o = v_{\text{WH}}$). We use the numerically measured values of the local flow velocity and sound speed, determined from the background flow Ψ_{bf} , which can be identified by a spatial WFT (despite the appearance of additional excitations). The WH horizon velocity is approximated by the speed of the left edge of $|\delta\Psi(x, t)|$ (see Fig. 3(a)(c)), while the BH horizon velocity is that of the step.

According to the mechanism illustrated in Fig. 3(a), the BCR has zero frequency in the WH frame, and the HR and the partner share its frequency in the BH frame. The BCR wavevector should therefore satisfy $\Delta\omega(\Delta k_{\text{BCR}}) = 0$ in the WH frame. This is indicated graphically by the intersection of the dashed red curve in Fig. 4(a) with the Δk axis, showing that $\Delta k_{\text{BCR}} \sim 2.5 \mu\text{m}^{-1}$. The frequency of BCR in the BH frame corresponds to $\Delta\omega = \pm\Delta k_{\text{BCR}}(v_{\text{BH}} - v_{\text{WH}}) = \pm 0.2$ rad/ms, indicated by the horizontal, dashed black lines, which intersect the solid red curve at the vertical lines $\pm\Delta k_{\text{BCR}}$. If the HR and partner modes are indeed stimulated by the BCR, they should fall on the intersection of these zero WH frequency lines with the solid blue and red curves respectively. The modes are labeled by “ u ” or “ v ”, according to the corresponding component of the BdG mode. Modes whose u -component has negative (positive) relative frequency in the step frame have negative (positive) energy relative to the condensate [6]. The BCR and partner modes thus have negative energy, while the Hawking mode has positive energy.

To capture the spectral properties of the modes observed in Fig. 3(c), and compare with the prediction in Fig. 4(a), we apply the spatial and temporal WFTs on $\Psi(x, t)$ and $\delta\Psi(x, t)$. On the LHS of the BH horizon

($x < x_{\text{BH}}$), we calculate the WFTs of $\Psi(x, t)$; on the RHS of the BH horizon ($x > x_{\text{BH}}$), we take $\delta\Psi(x, t)$ and multiply it by 10 to subtract the background and bring out the HR. The left panel of Fig. 4(b) shows the windowed frequency spectra [19] of $\Psi(x_I(t), t)$ ($\omega = 0\text{--}0.5$ rad/ms) and $\delta\Psi(x_O(t), t)$ ($\omega = 0.5\text{--}0.7$ rad/ms), in the BH horizon frame, along the red and blue lines in Fig. 3(c) with a Gaussian window of full-width 110 ms at $1/e$. The streak in the center corresponds to the background flow Ψ_{bf} , and indicates the approximate chemical potential $\mu \sim 0.36$ rad/ms. The two other streaks located symmetrically about the center correspond to HR ($\omega \sim 0.56$ rad/ms), and the BCR and the HR partner ($\omega \sim 0.15$ rad/ms). The full frequency spectra at $t = 650$ ms for x_I (red) and x_O (blue) are shown on the right panel.

The left panel of Fig. 4(c) shows the windowed wavevector spectrum as a function of position, in the laboratory frame. It is defined by WFTs of $\Psi(x, t_0)$ ($x < x_{\text{BH}}$) and $\delta\Psi(x, t_0)$ ($x > x_{\text{BH}}$) at $t_0 = 650$ ms, along the green line in Fig. 3(c), with a Gaussian window of full-width $42 \mu\text{m}$ at $1/e$ for Ψ , and $24 \mu\text{m}$ for $\delta\Psi$. The background flow spectrum between the horizons is centered on a large negative wavevector at each x , and extends from the BH to the WH horizon. The BCR spectrum is centered on large positive wavevectors, and is roughly the reflection of the background flow spectrum about $k = 0$. The HR and its partner mode spectra extend outward and inward from the BH horizon, with positive and negative wavevectors, respectively. The wavevector spectra at x_I (red) and x_O (blue) are shown on the right panel, with the modes labeled (except for v_{BCR}^*) in the figure.

We compare the WFT spectra (Fig. 4(b-c)) with the BdG dispersion relations (a) at x_I and x_O , corresponding to the intersections of the red and blue lines with the green line in Fig. 3(c). The numerical values of $\Delta\omega$ and Δk obtained from the WFT spectra of the GP solution are displayed in Table I, along with those predicted from the BdG dispersion relations. The GP spectra and BdG predictions agree to within 5%. Note that the flow is not perfectly stationary, so that the zero frequency of the initial BCR is not perfectly conserved. Also, the speed of the WH horizon changes slightly over time, which gives rise to the uncertainty in $\Delta\omega_{\text{BdG}}$ and Δk_{BdG} .

TABLE I. Numerical values of relative mode frequency $\Delta\omega$ (rad/ms) and wavevector Δk (μm^{-1}) from the GP Fourier spectra (FT) and from the WH-zero-frequency BdG dispersion relation (BdG). The uncertainty for the former is estimated by the widths of the Gaussians fitting the spectral peaks in Fig. 4(b-c), and the uncertainty for the latter is due to the variation of the speed of WH horizon.

Modes	$\Delta\omega_{\text{FT}}$	$\Delta\omega_{\text{BdG}}$	Δk_{FT}	Δk_{BdG}
u_{BCR}	-0.21(3)	-0.20 \pm 0.01	2.42(8)	2.45 \pm 0.02
u_{p}	-0.21(3)	-0.20 \pm 0.01	0.26(8)	0.26 \pm 0.01
u_{HR}	0.20(3)	0.20 \pm 0.01	0.65(12)	0.65 \pm 0.02

The spontaneous emission from a black hole horizon is

thermal, with temperature $T_{\text{H}} = \hbar\kappa/(2\pi k)$, where κ is the surface gravity [1, 2]. In the sonic analog, the surface gravity becomes $\kappa = d(v + c)/dx$, evaluated at the horizon [3]. When the radiation is stimulated, the flux ratio of the positive energy Hawking mode to the negative energy partner mode carries the signature of the thermal prediction [23, 24]. In particular, if $u_{\text{p}} = \alpha\hat{u}_{\text{p}}$ and $v_{\text{HR}} = \beta\hat{v}_{\text{HR}}$ are the BdG mode functions, with \hat{u} and \hat{v} normalized to unit flux, then the thermal prediction for a mode of frequency ω is $|\beta/\alpha| = \exp(-\pi\omega/\kappa)$. (To trim notational complexity, we here drop the Δ 's in front of ω and k , leaving implicit that these quantities are defined relative to the background flow.) In terms of the amplitudes extracted from the GP wavefunction, the β/α ratio is

$$\frac{|\beta|}{|\alpha|} = \frac{|v_{\text{HR}}|}{|u_{\text{p}}|} \frac{[|\frac{d\omega}{dk}|(1-D^2)/D^2]_{k_{\text{HR}}}^{1/2}}{[|\frac{d\omega}{dk}|(1-D^2)]_{k_{\text{p}}}^{1/2}}, \quad (3)$$

where $D = [\hbar\sqrt{c^2k^2 + \hbar^2k^4/4m^2} - \hbar^2k^2/2m - mc^2]/mc^2$ [25].

To test the thermal prediction we evaluate the mode amplitudes at a pair of points x_{p} and x_{HR} with a common retarded time, defined by phase velocity, at the BH horizon. These points are denoted by the magenta and cyan dots on the horizontal green line in Fig. 3(c). The common retarded time on the horizon is $t = 588$ ms, for which we find the surface gravity $\kappa \sim 350 \text{ s}^{-1}$ (using v and c computed directly from the GP wavefunction, see supplementary materials). The thermal prediction for $\omega = 200$ rad/s is $|\beta/\alpha| = 0.17_{-0.04}^{+0.05}$, allowing for a 5% uncertainty in ω and a 10% uncertainty in κ . This agrees reasonably well with the ratio 0.21 computed directly from the amplitudes according to Eq. 3.

Several factors could play a role in causing the GP ratio $|\beta/\alpha|$ to differ from the thermal prediction. First, the latter is exponentially sensitive to the value of κ , so the time dependence of κ can introduce a significant effect. Second, phonon dispersion can produce deviations that depend on how large are κ and ω compared to the sound speed over the healing length, $c/\xi \sim 320 \text{ s}^{-1}$, and on how wide is the linear regime of the function $c + v$ around the BH horizon ($\sim 6 \mu\text{m}$), compared to $c/\kappa \sim 1.2 \mu\text{m}$ [26]. And third, nonlinearity of the GP modes could lead to deviations from the linear prediction.

To conclude, we summarize the evidence that the black hole laser effect plays no role in our GP simulations. First, we find the unstable mode grows in proportion to the square of the background flow density, which is unrelated to lasing action. Second, the growing mode has zero frequency in the WH frame, which is unrelated to the frequency of the fastest growing unstable cavity mode of the black hole laser [25]. And third, because the WH horizon recedes from the BH horizon, the most unstable cavity mode shifts with time, so the condition for lasing action is not met.

We thank R. Parentani for numerous helpful discussions and suggestions. This material is based upon

work supported by the U.S. National Science Foundation Physics Frontier Center at JQI and grants PHY-

1407744, PHY-1004975 and PHY-0758111, and by the Army Research Office Atomtronics MURI .

-
- [1] S. W. Hawking, *Nature* **248**, 30 (1974).
 - [2] S. Hawking, *Communications in Mathematical Physics* **43**, 199 (1975).
 - [3] W. G. Unruh, *Phys. Rev. Lett.* **46**, 1351 (1981).
 - [4] L. J. Garay, J. R. Anglin, J. I. Cirac, and P. Zoller, *Phys. Rev. Lett.* **85**, 4643 (2000).
 - [5] S. Corley and T. Jacobson, *Phys. Rev. D* **59**, 124011 (1999).
 - [6] J. Macher and R. Parentani, *Phys. Rev. A* **80**, 043601 (2009).
 - [7] A. Recati, N. Pavloff, and I. Carusotto, *Phys. Rev. A* **80**, 043603 (2009).
 - [8] C. Mayoral, A. Recati, A. Fabbri, R. Parentani, R. Balbinot, and I. Carusotto, *New Journal of Physics* **13**, 025007 (2011).
 - [9] P.-E. Larré, A. Recati, I. Carusotto, and N. Pavloff, *Phys. Rev. A* **85**, 013621 (2012).
 - [10] S. J. Robertson, *Journal of Physics B: Atomic, Molecular and Optical Physics* **45**, 163001 (2012).
 - [11] A. Coutant, R. Parentani, and S. Finazzi, *Phys. Rev. D* **85**, 024021 (2012).
 - [12] C. J. Zhu, L. Deng, E. W. Hagley, and M.-L. Ge, *Phys. Rev. Lett.* **113**, 090405 (2014).
 - [13] D. Boiron, A. Fabbri, P.-E. Larré, N. Pavloff, C. I. Westbrook, and P. Ziñ, *Phys. Rev. Lett.* **115**, 025301 (2015).
 - [14] J. Steinhauer, *Nature Physics* **10**, 864 (2014).
 - [15] I. Carusotto, S. X. Hu, L. A. Collins, and A. Smerzi, *Phys. Rev. Lett.* **97**, 260403 (2006).
 - [16] A. Coutant, A. Fabbri, R. Parentani, R. Balbinot, and P. Anderson, *Phys. Rev.* **D86**, 064022 (2012).
 - [17] X. Busch, F. Michel, and R. Parentani, *Phys. Rev.* **D90**, 105005 (2014).
 - [18] M. Tettamanti, S. L. Cacciatori, A. Parola, and I. Carusotto, (2016), arXiv:1603.04702.
 - [19] J. Gomes and L. Velho, *From Fourier Analysis to Wavelets (Course Notes)* (Instituto de Matemática Pura e Aplicada, IMPA, 1999).
 - [20] P. Leboeuf and N. Pavloff, *Phys. Rev. A* **64**, 033602 (2001).
 - [21] I. Carusotto and G. Rousseaux, *Proceedings, 9th SIGRAV Graduate School in Contemporary Relativity and Gravitational Physics on Analogue Gravity Phenomenology*, *Lect. Notes Phys.* **870**, 109 (2013).
 - [22] C. Pethick and H. Smith, *Bose-Einstein Condensation in Dilute Gases*, 2nd ed., Vol. 2 (Cambridge, 2001).
 - [23] W. G. Unruh, *Phys. Rev.* **D51**, 2827 (1995).
 - [24] W. G. Unruh, *Proceedings, Horizons of Quantum Physics*, *Found. Phys.* **44**, 532 (2014).
 - [25] S. Finazzi and R. Parentani, *New Journal of Physics* **12**, 095015 (2010).
 - [26] S. Finazzi and R. Parentani, *Phys. Rev. D* **85**, 124027 (2012).
 - [27] L. Salasnich, A. Parola, and L. Reatto, *Phys. Rev. A* **65**, 043614 (2002).
 - [28] P. Muruganandam and S. Adhikari, *Computer Physics Communications* **180**, 1888 (2009).
-

Supplemental Material: Mechanism of stimulated Hawking radiation in a laboratory Bose-Einstein condensate

The supplemental material for the above paper is composed of five sections. Section I describes simulations of the experiment of Ref. [14]. Section II presents a description of the windowed Fourier transform (WFT). Section III describes the procedure for separating the excitation modes from the underlying average condensate wavefunction. Section IV recounts the search for BEC parameter regimes in which Hawking radiation can be observed with well-resolved wavelengths and frequencies. Section V describes the Bogoliubov-de Gennes mode analysis used in our paper.

I. CHARACTERIZATION OF THE EXPERIMENTAL CONDENSATES AND DESCRIPTION OF SIMULATION PROCEDURES

To determine the wave function of the initial condensate in Ref. [14] we used the time-dependent Gross-Pitaevskii (GP) equation in 1D and 3D:

$$i\hbar \frac{\partial \Psi(\mathbf{r}, t)}{\partial t} = \left(-\frac{\hbar^2}{2m} \nabla^2 + V(\mathbf{r}, t) + g_{3D} N |\Psi|^2 \right) \Psi(\mathbf{r}, t). \quad (1)$$

where N is the number of condensate atoms, m is the mass of a condensate atom, $g_{3D} = 4\pi\hbar^2 a/m$ where a is the s -wave scattering length, and $V(\mathbf{r}, t)$ is the full external potential which is given by

$$V(\mathbf{r}, t) = U(\mathbf{r}) + U_{\text{step}}(\mathbf{r}, t). \quad (2)$$

The potential in which the initial condensate was formed in the experiment of Ref. [14] is denoted by $U(\mathbf{r})$ and $U_{\text{step}}(\mathbf{r}, t)$ is the potential for the step that was swept along the length of the condensate in the experiment, as shown schematically in Fig. 1 of our paper. Here we describe how we determined $V(\mathbf{r}, t)$ and $\Psi(\mathbf{r}, 0)$, so as to solve Eq. 1 as an initial-value problem.

The wave function for the initial condensate, $\Psi_0(\mathbf{r})$, satisfies the time-independent GP equation:

$$\left(-\frac{\hbar^2}{2m} \nabla^2 + U(\mathbf{r}) + g_{3D} N |\Psi_0(\mathbf{r})|^2 \right) \Psi_0(\mathbf{r}) = \mu_0 \Psi_0(\mathbf{r}), \quad (3)$$

where μ_0 is the chemical potential of the ground-state condensate.

In order to determine $\Psi_0(\mathbf{r})$ we first found the potential, $U(\mathbf{r})$, that is produced by the red-detuned trapping laser specified in Ref. [14]. There, the laser beam characteristics are stated in terms of its wavelength, $\lambda = 812$ nm, and the beam waist, $w_0 = 5$ mm. We used this data to model the trapping laser light as a focused ideal Gaussian laser beam. Thus the trapping potential is proportional to the beam intensity:

$$U(\mathbf{r}) = U_0 \left[1 - \left(\frac{w_0}{w(x)} \right)^2 \exp \left(\frac{-2\rho^2}{w^2(x)} \right) \right]. \quad (4)$$

where x is the axis of light propagation, $\rho = \sqrt{y^2 + z^2}$ is the transverse (axial) radial coordinate, w_0 is the beam waist, U_0 is proportional to the peak laser intensity and

$$w(x) = w_0 \sqrt{1 + \left(\frac{x}{x_0} \right)^2}, \quad \text{where } x_0 = \frac{\pi w_0^2}{\lambda}. \quad (5)$$

We have chosen the origin of energy so that $U(\mathbf{r})$ vanishes at the center of the trap, $U(0) = 0$. Reference [14] also states that, since the long axis of the needle-shaped condensate lies in a horizontal plane, the effect of gravity is mostly (all but 9%) compensated for by an external magnetic field with a vertical gradient. For simplicity, in our model we take the gravitational and compensating magnetic forces to cancel exactly.

Specification of the wavelength and beam waist fixes all the parameters in $U(\mathbf{r})$ except for U_0 . Reference [14] gives the axial trap frequency as $\omega_\rho/2\pi = 123$ Hz. We used this frequency to determine U_0 by expanding $U(\mathbf{r})$ to second order about $\mathbf{r} = 0$:

$$U(\mathbf{r}) \approx \left(\frac{2U_0}{w_0^2} \right) \rho^2 + \left(\frac{U_0}{x_0^2} \right) x^2 \equiv \frac{1}{2} m \omega_\rho^2 \rho^2 + \frac{1}{2} m \omega_x^2 x^2. \quad (6)$$

Thus $U_0 = (1/4)m\omega_\rho^2 w_0^2 \approx 39 \text{ k nK}$, where k is the Boltzmann constant. This completes our determination of $U(\mathbf{r})$ from the experimental parameters.

The number of atoms in the condensate, N , is not explicitly stated in Ref. [14], but it can be inferred from the chemical potential and the trap parameters.

Although Ref. [14] does not provide a stated estimate of the value(s) of N used in the experiments, but indicates that μ_0/k was measured to be 8 nK. The value of μ_0 is uniquely determined by the trap potential and the value of N . Thus one can construct a table connecting μ_0 and N , by solving Eq. (3) numerically for a range of N values, *e.g.* by integrating Eq. (1) in imaginary time to find the condensate ground state and the corresponding chemical potential as functions of N . However, for this potential, μ_0 is a relatively insensitive function of N . This is shown in Fig. (1) which contains optical-density images of the solutions of Eq. (3) for atom numbers ranging from $N = 2000$ to 6000. For $\mu_0/k = 8.5 \text{ nK}$ ($N = 2000$), the condensate which about $40 \mu\text{m}$ long. Figure 2 of Ref. [14] shows images that are at least 50% longer. Thus we estimate $N = 6000$ atoms, for which $\mu_0/k = 10.4 \text{ nK}$ in our model potential. This gives a better match of the length of our condensate to that determined experimentally. The experimental data are not accompanied with uncertainty analysis.

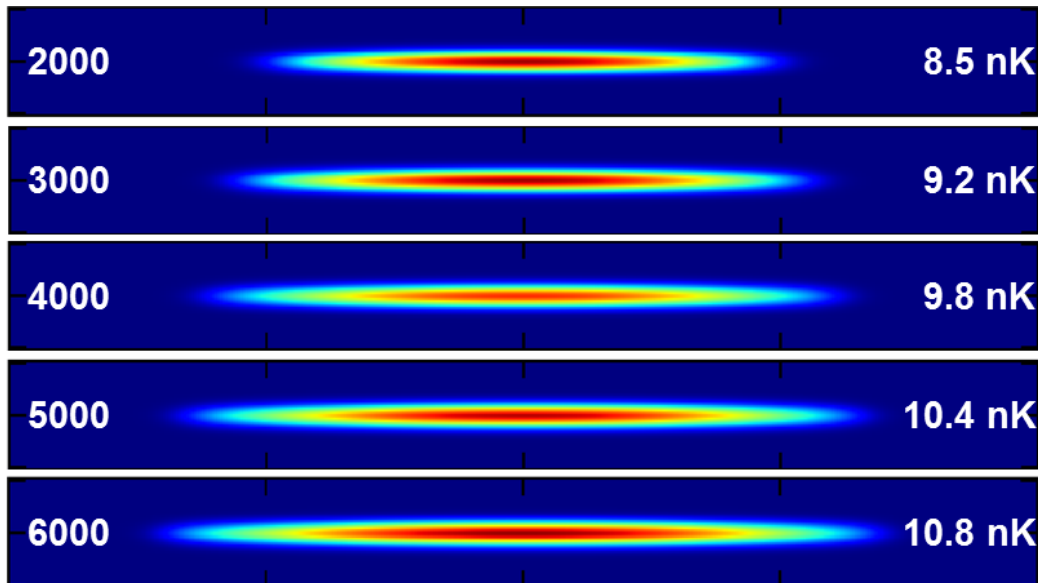


FIG. 1. Optical densities of condensate ground state from GP simulation for atom numbers $2000 < N < 6000$ as labeled on left, corresponding to the values of chemical potential μ/k as labelled on the right. Full horizontal and vertical scales are 100 and 12 microns, respectively.

We also note that $\omega_x = \omega_\rho w_0 / (\sqrt{2}x_0) \approx 0.037\omega_\rho = (2\pi) \times 4.5 \text{ Hz}$. Thus $\omega_x \ll \omega_\rho$, which justifies treating the system as one of one-dimensional BEC dynamics in the coordinate x . We have verified this by comparison of results of numerical solutions of one- and three-dimensional Gross-Pitaevski equations for the system.

TABLE I. Parameters of the trapped BEC as reported in, or inferred from (*), Ref. [14]. Uncertainties are not stated in Ref. [14], and we do not attempt to estimate them in this work.

Parameter	Value	Units
atom	^{87}Rb	
atomic state	$F = 2, M_F = 2$	
trapping laser wavelength λ	812	nm
beam waist w_0	5	micron
radial trap frequency ν	123	Hz
transverse energy level spacing E	6	nK k
healing length ξ	2	micron
nominal chemical potential μ	8	nK k
*actual chemical potential μ	10.4	nK k
*axial length scale x_0 from eq. (5)	97	micron
*number of condensate atoms N	6000	atoms

A. Reduction to a one-dimensional system

In Ref. [14], the condensate is tightly confined in the transverse radial direction, and thus can be approximated by a quasi-one-dimensional wavefunction. We approximate the wavefunction in the radial direction by the solution of a harmonic oscillator, such that

$$\Psi(\mathbf{r}, t) = \frac{\exp[-\rho^2/(2d^2)]}{d\sqrt{\pi}} \Psi_{1D}(x, t), \quad (7)$$

where $d = \sqrt{\hbar/(m\omega_\rho)}$. Integrating the 3D GP equation over the Cartesian coordinates y and z , we obtain a 1D GP equation with an effective interaction coefficient $g_{1D} = g_{3D}m\omega_\rho/\hbar$:

$$i\hbar \frac{\partial \Psi_{1D}(x, t)}{\partial t} = \left(-\frac{\hbar^2}{2m} \frac{\partial^2}{\partial x^2} + V(x, t) + g_{1D}N |\Psi_{1D}(x, t)|^2 \right) \Psi_{1D}(x, t). \quad (8)$$

where \hbar is the Planck constant and $V(x, t)$ is the full external potential $V(\mathbf{r}, \mathbf{t})$ evaluated at $y = z = 0$. We define the coefficient of the nonlinear term as, $g = g_{1D}N$.

We take the number of atoms determined by the 3D GP equation, $N = 6000$, and use Eq. 8 to simulate the step-sweeping experiment. Note that Ref. [18] simulated the dynamics by using a 1D nonpolynomial nonlinear Schrodinger equation (NPSE) [27], which incorporates the effect of a variable axial density on the transverse shape of the GP wave function (under the condition that the axial derivative of the transverse wave function is much smaller than the transverse derivative). Here we use a simpler 1D GP equation, which assumes a fixed transverse shape of the wave function. Also, note that in the paper and other sections in this supplemental material, we drop the subscript “1D” in $\Psi_{1D}(x, t)$ while mentioning the 1D GP wavefunction.

B. Solution of the time-dependent 1D GP equation

The time-dependent 1D GP equation is solved by using the split-step Crank-Nicholson algorithm [28] on a 1D spatial grid of $320 \mu\text{m}$ with 4800 points, first propagating in imaginary time to obtain the initial stationary condensate, then propagating in real time with the given initial state to simulate the dynamics. To simulate the step-sweeping experiment [14], we use a step potential $U_{\text{step}}(x, t)$, which takes the form

$$U_{\text{step}}(x, t) = -U_s \Theta(x_s(t) - x), \quad (9)$$

where Θ is Heaviside’s step function; U_s is the step strength, which takes the values of $U_s/k = 3 \text{ nK}$ and 6 nK ; $x_s(t)$ represents the step location, moving at a constant speed, $v_s = 0.21 \text{ mm/s}$.

II. WINDOWED FOURIER TRANSFORM

Here we summarize the basic ideas of the windowed Fourier transform (WFT), and explain our use of it. In II A, we give the definition of WFT used here, and provide a few basic examples to show how it can resolve spectral information on non-stationary phenomena. In II B, we describe the application of the WFT to the determination of flow and sound speeds, $v(x)$ and $c(x)$, in inhomogeneous media. In II C, we discuss calculations of the wavevector and frequency spectra displayed in Fig. 4(b-c) of the main text, and the additional spectra that distinguish the partner and BCR modes. In II D, we show the windowed frequency spectrum for the experimental regime, and a comparison with the dispersion relation.

A. Definition and examples

A windowed Fourier transform [19] $f(k, x)$ of a function $f(x)$ is defined as:

$$f(k, x) = \int_{-\infty}^{\infty} dy f(y) w(y - x; D) e^{-iky}, \quad (10)$$

where $w(y - x; D) = \exp(-(y - x)^2/D^2)/(\sqrt{\pi}D)$ is a Gaussian window function of width D . With the filtering of the window, the transformed function $f(k, x)$ constitutes a local Fourier transform of $f(x)$, capturing features that vary

on length scales much smaller than D . For a plane wave with wavevector q and amplitude f_q , $f(x) = f_q \exp(iqx)$, the transformed function is $f(k, x) = f_q \exp(-(k - q)^2(D/2)^2)$: a Gaussian in k -space, centered at $k = q$ with width $2/D$ and peak amplitude f_q .

Suppose now that $f(x) = f_q(x) \exp(iqx)$, where $f_q(x)$ has weak dependence on x , and can be adequately approximated near a point x_0 by

$$f_q(x) = f_q(x_0) + f'_q(x_0)(x - x_0). \quad (11)$$

Then for sufficiently small values of D , the WFT of $f(x)$ near $x = x_0$ is approximately

$$f(k, x) \approx f_q(x_0) e^{-(k-q)^2(D/2)^2} + f'_q(x_0) i \frac{k-q}{2} D^2 e^{-(k-q)^2(D/2)^2}. \quad (12)$$

Note that the second term vanishes at the peak position $k = q$, so that $f(q, x_0) \approx f_q(x_0)$.

Finally, let $f(x)$ be composed of a number of such slowly-varying modes,

$$f(x) = \sum_n f_{q_n}(x) e^{iq_n x}, \quad (13)$$

so that Eq. 12 becomes

$$f(k, x_0) \approx \sum_n \left[f_{q_n}(x_0) + f'_{q_n}(x_0) \left(i \frac{k - q_n}{2} D^2 \right) \right] e^{-(k - q_n)^2(D/2)^2}. \quad (14)$$

In k -space, each mode presents a Gaussian distribution centered on its respective q_n , whose peak value of $f(q_n, x_0)$ defines the local mode amplitude. This is how we make quantitative determinations of the mode amplitudes that are discussed in our paper.

B. Determination of the profiles of flow speed and the speed of sound

As shown in the paper, during the sweep of the step, the time-dependent GP wavefunction $\Psi(x, t)$ exhibits excitation modes on top of the background condensate. To calculate the speed of sound $c(x)$ and flow speed $v(x)$, we resolve the background condensate flow by applying a WFT.

First, the amplitude of the background flow at a given time t_0 can be calculated by applying a spatial WFT on the GP density $|\Psi(x, t_0)|^2 = n(x)$, where t_0 is suppressed for brevity.

$$n(k, x) = \int_{-\infty}^{\infty} dy n(y) w(y - x; D) e^{-iky}. \quad (15)$$

Fig. 2(a) shows the result of a spatial WFT of density $n(x)$ (which corresponds to Fig. 2(e) in the paper) with width $D = 5 \mu\text{m}$. The central streak at $k \sim 0$ corresponds to the background flow, whose peak value gives rise to the background density $n_{\text{bf}}(x) = |n(k \sim 0, x)|$, as shown in Fig. 2(b). The local speed of sound can then be expressed as by $c(x) = \sqrt{g n_{\text{bf}}(x)/m}$. In Fig. 2(b), we see that WFT works quite well in the slowly varying regions away from the two horizons: in the exterior region, $n_{\text{bf}}(x)$ matches the GP density $n(x)$; in the interior region, $n_{\text{bf}}(x)$ is at about the center of spatial oscillations. Near the event horizons, the background density changes rather quickly, such that WFT fails to estimate the correct local amplitude, and the resulting $n_{\text{bf}}(x)$ is smoothed out nearby these regions.

Second, the flow velocity can be calculated by a WFT of the GP wavefunction

$$\Psi(k, x) = \int_{-\infty}^{\infty} dy \Psi(y) w(y - x; D) e^{-iky}, \quad (16)$$

where again t_0 is suppressed for brevity. Fig. 2(c) shows the windowed wavevector spectrum $|\Psi(k, x)|^2$ with width $D = 5 \mu\text{m}$. The dominant streak is the background flow, whose peak location $k_{\text{bf}}(x)$ gives rise to the flow velocity in the rest frame of the step, $-v(x) = \hbar k_{\text{bf}}(x)/m - v_s$, as shown in Fig. 2(d); the peak value of the streak corresponds to $n_{\text{bf}}(x) = |\Psi(k_{\text{bf}}, x)|^2$, which also gives the speed of sound $c(x)$, and is later used for the dispersion relation Eq. 30. In addition, we calculate the velocity profile by using the full GP wavefunction, $v_{\text{GP}}(x) = \hbar/(mn(x)) \text{Im}[\Psi^*(x) d\Psi(x)/dx] - v_s$. We can see that WFT works well in regions apart from the event horizons, and effectively projects out the spatial oscillation present in $v_{\text{GP}}(x)$.

Fig. 2(e-f) compares $v(x)$ and $c(x)$ from the windowed spectra (panel (e)) with those obtained from the full GP wavefunction (panel (f)). In short, near the event horizon, the approach of directly adopting the GP wavefunction gives more accurate speed profiles, with the correct horizon locations and the respective surface gravity; yet away from the horizons, the WFT effectively removes excitations from the background flow, and hence gives a more suitable definition for $v(x)$ and $c(x)$.

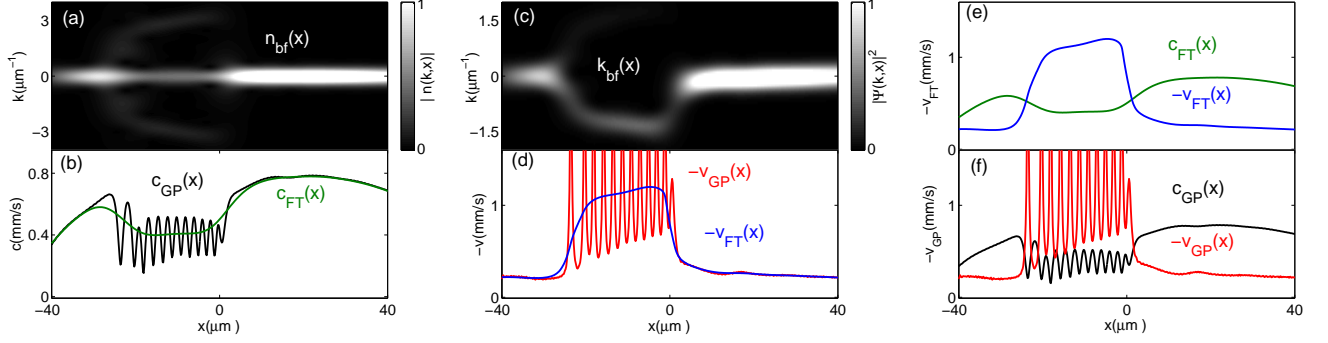


FIG. 2. Determination of flow speed $v(x)$ and the speed of sound $c(x)$. (a) windowed wavevector spectrum of density $n(x)$ at $t_0 = 80$ ms (Fig. 2(e) in the paper); (b) black: local speed of sound c_{GP} from total density $n(x)$; green: speed of sound c_{FT} from the background flow density $n_{bf}(x)$, filtered with the Fourier spectrum; (c) windowed wavevector spectrum of GP wavefunction $\Psi(x)$; (d) red: windowed flow speed, v_{GP} , from a direct calculation on $\Psi(x)$; blue: flow speed v_{FT} from the background flow wavevector $k_{bf}(x)$; panels (e-f): flow structure determined by the Fourier spectra (e) and that directly obtained from the GP wavefunction (f).

C. Spectral analysis with windowed Fourier transform

The spectral properties of excitation modes can be obtained by performing spatial and temporal WFTs on the condensate wavefunction. Given a GP wavefunction, $\Psi(x, t)$, we calculate its local wavevector spectrum and frequency spectrum by applying the WFTs. To obtain a local wavevector spectrum, we perform a spatial WFT on the wavefunction $\Psi(x, t_0)$ using Eq. 16 at a time t_0 at which the mode amplitudes have grown sufficiently large. The result is presented in Fig. 4(c) in the paper, in which the excitation modes are resolved in addition to the background flow. Note that for the region on the RHS of the step, we perform the WFTs on the variation function $\delta\Psi(x, t)$ rather than $\Psi(x, t)$ (see Sec. III), in order to subtract the background component and bring out the excitation mode in that region.

For a local frequency spectrum, we apply a temporal WFT at position $x_0(t)$ moving at constant speed v_s with the potential step:

$$\Psi(\omega, t) = \int_{-\infty}^{\infty} d\tau \Psi(x_0(\tau), \tau) w(\tau - t; T) e^{i\omega\tau}, \quad (17)$$

where $w(\tau - t; T)$ represents a Gaussian window function of width T , $w(\tau - t; T) = e^{-(\tau - t)^2/T^2}/\sqrt{\pi}T$; x_0 is selected to be both inside (x_I) and outside the BH cavity (x_O), which is indicated by the red and blue lines in Fig. 3(c) of the paper. The result is presented in Fig. 4(b) in the paper. In the figure, there are two modes (ψ_p and ψ_{BCR}) overlapped in the frequency spectrum ($\omega \sim 0.15 \mu\text{m}$) evaluated at position $x_I(t)$. To resolve the two modes, we perform a spatial WFT evaluated at $x_I(t)$ for various times

$$\Psi(k, t) = \int_{-\infty}^{\infty} dy \Psi(y, t) w(y - x_I(t); D) e^{-iky}. \quad (18)$$

The result is presented in Fig. 3(a), from which ψ_{BCR} and ψ_p are separated at different wavevectors, k_{BCR} (solid red line) and k_p (dashed red line). Furthermore, by performing a temporal WFT on $\Psi(k, t)$ at the given wavevectors, we resolve the overlapped streaks in the initial frequency spectrum at $\omega \sim 0.15$ rad/ms, as shown in Fig. 3(b-c).

D. Windowed frequency spectrum for the experimental regime

In Fig. 4 of the paper, we presented a full spectral analysis for the modified regime, which agrees with the prediction from the dispersion relations. Here we present the frequency spectrum for the experimental regime. This shows that no black hole laser effect is apparent in our simulation of the experiment of Ref. [14].

We apply the temporal WFT on $\Psi(x, t)$ at a position about the center of the cavity, $x_I = x_{BH} - 12 \mu\text{m}$, indicated by the red line in Fig. 3(b) of the paper. The resulting frequency spectrum is given in Fig. 4. The streak that appears from early times shows the frequency of the background flow wavefunction Ψ_{bf} . The lower streak corresponds to the superposition of the BCR and the partner mode. The cut-through at $t = 100$ ms is shown in panel (b), from which the relative frequency (of the u -components) $\Delta\omega \sim -0.11$ rad/ms.

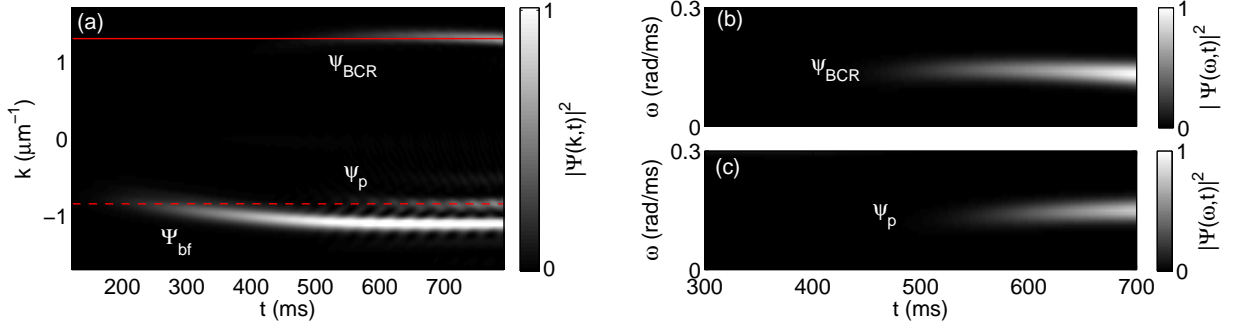


FIG. 3. Distinguishing the BCR mode (ψ_{BCR}) and the partner mode (ψ_p). (a) Local wavevector spectrum evaluated at $x_I(t)$ for various times, in which the BdG modes (ψ_{BCR} and ψ_p) of the same frequency are separated at different k values; (b) the frequency spectrum of $\Psi(k_{\text{BCR}}, t)$, where k_{BCR} is indicated by the solid red line in (a); (c) the frequency spectrum of $\Psi(k_p, t)$, with k_p indicated by the dashed red line in (a).

We also predict this relative frequency using the dispersion relation (as Fig. 4(a) of the paper, with details given in Sec. V B). The assumption that the BCR is the zero-frequency mode in the WH horizon frame determines $\Delta k_{\text{BCR}} = 2.9 \mu\text{m}^{-1}$. Taking into account the velocity difference between the WH and BH horizons, $v_{\text{BH}} - v_{\text{WH}} \sim 0.032 \text{ mm/s}$, the relative frequency of BCR (and the HR pair) in the BH horizon is given by $\Delta\omega = \pm\Delta k_{\text{BCR}}(v_{\text{BH}} - v_{\text{WH}}) \sim \pm 0.09 \text{ rad/ms}$, which is indicated by the dashed black lines in panel (c). This predicted frequency differs from the measured value from the WFT by 16 %.

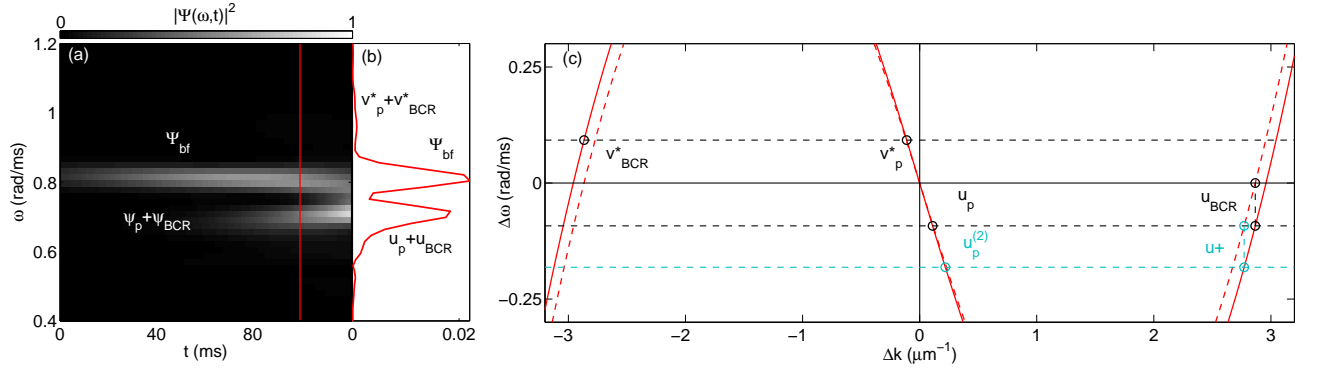


FIG. 4. Windowed frequency spectrum and dispersion relation for the experimental regime. (a) frequency spectrum evaluated at $x = x_{\text{BH}} - 12 \mu\text{m}$. (b) cut-through along the red line in (a). (c) dispersion relations in the WH (dashed red) and BH (solid red) reference frames, evaluated at $t = 100 \text{ ms}$. The dashed black lines show the frequencies of the BCR mode in the BH horizon frame, which stimulates the first HR pair. The dashed cyan line indicates the frequency of a positive-norm mode ψ_+ in the BH horizon frame, which stimulates the second HR pair. Note that u_+ represents the u-component of ψ_+ (Eq. 22); u_p and $u_p^{(2)}$ denote the u-components of the first and the second partner mode, respectively.

The wavelength of the partner mode predicted using the dispersion relation is $\lambda_p \sim 57 \mu\text{m}$, which is greater than the width of the supersonic cavity $L \sim 25 \mu\text{m}$. Therefore the partner cannot be treated in the WKB approximation, and the discrete spectrum of cavity modes modifies the emission, unlike in the M2 regime where the ratio λ_p/L is smaller. This may explain the irregular emission of the HR in the experimental regime shown in Fig. 3(b) of the paper.

In addition, we find that the lasing effect will not take place in the experimental regime, where the WH horizon recedes from the BH horizon. When the partner mode scatters at the WH horizon, it creates a pair of positive-norm (ψ_+) and negative-norm (ψ_-) modes [14] (here we only show the former, u_+ in panel (c)), whose frequency in the WH frame is that of the partner. Due to relative velocity between the two horizons, ψ_+ has a frequency in the BH horizon frame, indicated by the dashed cyan line in Fig. 4(c), that is lower than the frequency of the first partner mode, and stimulates a HR pair at that shifted frequency. Therefore, self-amplification will not occur.

III. SEPARATION OF FAST AND SLOW OSCILLATION OF CONDENSATE WAVEFUNCTION

To separate the HR from the subsonic background flow, we apply a smoothing procedure to separate fast oscillatory modes from the slowly-varying components in the GP wavefunction. The procedure is equivalent to calculating the moving average of a discrete data set, which smooths out short-term fluctuations. Here the moving average of wavefunction $\Psi(x)$ is defined as

$$\bar{\Psi}(x) = \frac{1}{2D} \int_{x-D}^{x+D} dy \Psi(y), \quad (19)$$

where the integral serves as a square window of width $2D$ centered at x , over which $\Psi(x)$ is being averaged. For components in $\Psi(x)$ with wavelength much shorter than D (i.e. $D \gg \pi/k$), the integral would give rise to an average of zero, leaving those that are slowly varying in space (i.e. $\pi/k \gg D$) in $\bar{\Psi}(x)$.

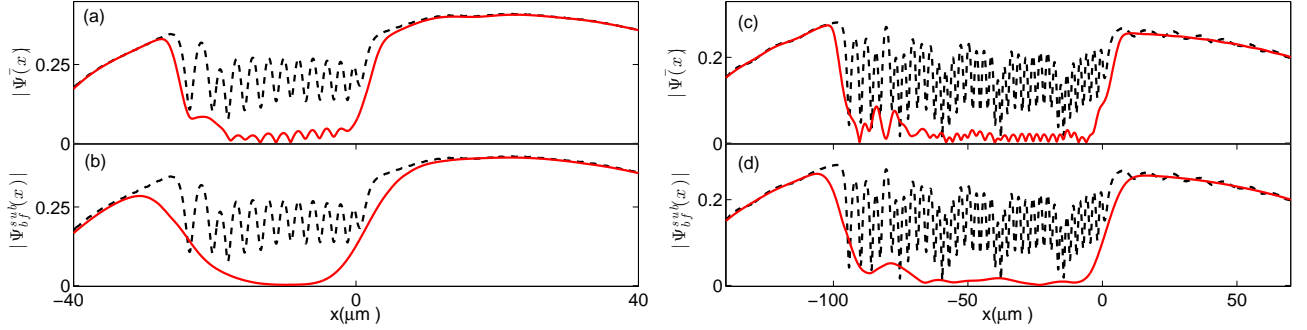


FIG. 5. Comparison of the smoothed wavefunction (panels (a)(c)), $\bar{\Psi}$, with subsonic background flow, $\Psi_{\text{bf}}^{\text{sub}}$, obtained by a spatial WFT (panels (b)(d)). Experimental regime (Fig. 2(e) in the paper): (a) smoothed wavefunction using Eq. 19 with window width $D = 5.4 \mu\text{m}$; (b) spatial WFT $|\Psi(k, x)|$ with Gaussian width $D = 5 \mu\text{m}$ evaluated at $k \sim 0$. Modified regime (Fig. 3(d) in the paper): (c) smoothed wavefunction using Eq. 19 with window width $D = 11.4 \mu\text{m}$; (d) spatial WFT $|\Psi(k, x)|$ with Gaussian width $D = 7 \mu\text{m}$ evaluated at $k \sim 0$. Note that the dashed black curve in all the panels corresponds to the GP wavefunction, $|\Psi(x)|$.

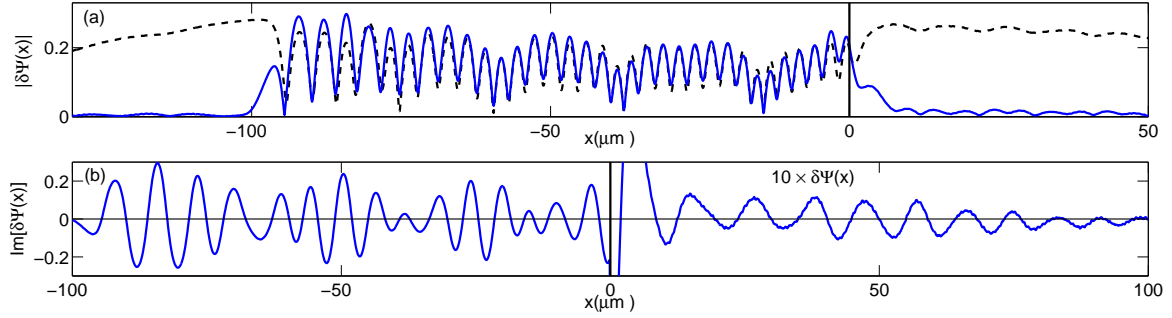


FIG. 6. Variation function in the M2 regime, $\delta\Psi(x)$, calculated with window width $D = 11.4 \mu\text{m}$. (a) blue: $|\delta\Psi(x)|$; dashed black: $|\Psi(x)|$. (b) blue: imaginary part of $\delta\Psi(x)$, whose value on the RHS of the step (denoted by the vertical black line) is multiplied by 10.

According to Fig. 2(c), the background flow in the subsonic region ($\Psi_{\text{bf}}^{\text{sub}}$) has $k \sim 0$ and can be separated from the GP wavefunction through Eq. 19, such that $\bar{\Psi}(x) \approx \Psi_{\text{bf}}^{\text{sub}}(x)$. Furthermore, highly oscillatory components in the wavefunction, including all the excitation modes (ψ_j) and the supersonic background flow ($\Psi_{\text{bf}}^{\text{sup}}$), can be obtained by subtracting the GP wavefunction with the non-oscillatory component, $\delta\Psi(x) = \Psi(x) - \bar{\Psi}(x)$. Thus, the variation $\delta\Psi(x)$ can be expressed as

$$\delta\Psi \approx \psi_p + \psi_{\text{HR}} + \psi_{\text{BCR}} + \Psi_{\text{bf}}^{\text{sup}}. \quad (20)$$

Figs. 5(a)(c) show the application of Eq. 19 to obtain a smoothed profile of $|\bar{\Psi}(x)|$ in the experiment of Ref. [14], and for a simulation in the M2 regime that is discussed in Sec. IV. A separate calculation using the spatial WFT is shown

in Fig. 3(b)(d), in which $|\Psi_{\text{bf}}^{\text{sub}}|$ is evaluated by taking the peak amplitude $|\Psi(k, x)|$ at $k \sim 0$. Both approaches agree with the GP wavefunction at regions away from the event horizons, capturing the background component outside the BH cavity (the region between the BH and WH horizons). This gives rise the variation function $\delta\Psi(x)$, which nicely approximates the components in Eq. 20. Fig. 6 shows the variation $\delta\Psi(x)$ for the M2 regime, which agrees with the GP wavefunction inside the BH cavity. Note that in Fig. 6(b) we have multiplied $\delta\Psi(x)$ by a factor of 10 for $x > x_{\text{BH}}$ to bring out the the HR mode in the exterior region.

IV. BEC PARAMETER REGIMES IN WHICH HAWKING RADIATION HAS GREATER VISIBILITY

To find a more distinctive signature of HR, we study the GP evolution in different parameter regimes where the frequency of the trapping potential, ω_x , and the depth, U_s , and speed, v_s , of the potential step are varied away from the values (ω_x^0 , U_s^0 , v_s^0) reported in Ref. [14], which are recorded in Sec. I. We find that by choosing an appropriate set of experimental parameters, the HR can be observed with well-resolved wavelengths and frequencies.

Fig. 7 shows four representative cases for our investigation. Regimes E1 and E2 use the same trapping frequency as the experimental value ω_x^0 , but adopt a greater step speed $v_s = 1.5v_s^0$; case E1 uses the same step strength as Fig. 3(b) in the paper, $U_s/k = 6$ nK; case E2 has a greater step strength, $U_s/k = 9$ nK. Note that ω_x^0 and v_s^0 are the reference values taken from [14], $\omega_x^0 = (2\pi) \times 4.5$ Hz, and $v_s^0 = 0.21$ mm/s.

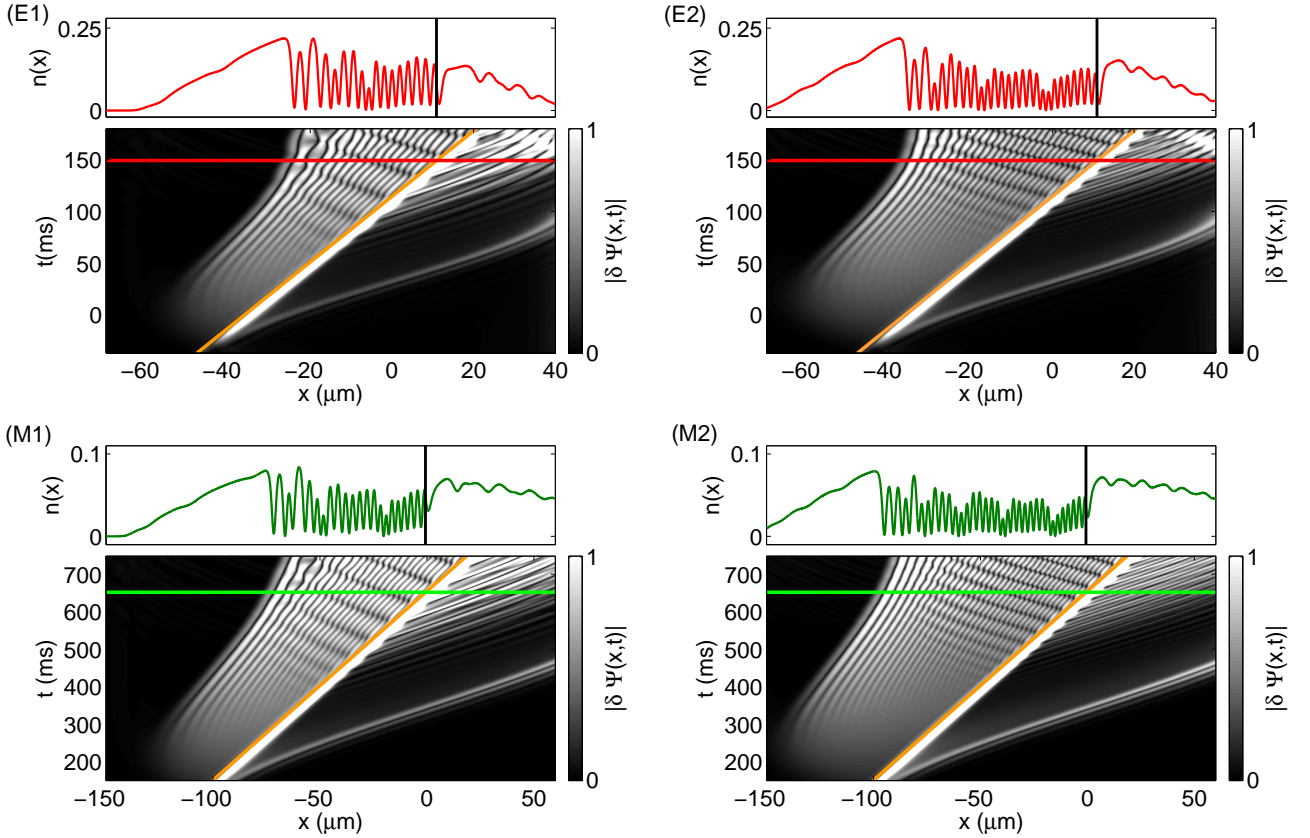


FIG. 7. Time evolution for modified parameter regimes, characterized by modified trapping frequency $\omega_x = \gamma\omega_x^0$, step speed $v_s = 1.5\gamma^{1/3}v_s^0$, and step strength U_s . Note that ω_x^0 and v_s^0 are the reference values taken from [14], $\omega_x^0 = (2\pi) \times 4.5$ Hz, and $v_s^0 = 0.21$ mm/s. Modified regimes: (E1) $\gamma = 1$, $U_s/k = 6$ nK and $v_s = 1.5v_s^0$; (E2) $\gamma = 1$, $U_s/k = 9$ nK, and $v_s = 1.5v_s^0$; (M1) $\gamma = 1/4$, $U_s/k = \gamma^{2/3} \times 6$ nK, $v_s = 1.5\gamma^{1/3}v_s^0$; (M2) $\gamma = 1/4$, $U_s/k = \gamma^{2/3} \times 9$ nK, $v_s = 1.5\gamma^{1/3}v_s^0$. Bottom: time evolution of $|\delta\Psi(x, t)|$; top: density profile $n(x)$ at times indicated by the horizontal red (green) line in the lower panel. Note that $|\delta\Psi(x, t)|$ is multiplied by 10 for $x > x_{\text{BH}}$, where x_{BH} is indicated by the solid orange lines.

Regimes M1 and M2 are the cases equivalent to E1 and E2 with a modified trapping frequency, $\omega_x = (1/4)\omega_x^0$. Here we use some scaling relations to determine the step speed v_s and depth U_s that give rise to an equivalent flow

structure while varying the trapping frequency. We know that modifying ω_x changes the speed of sound c (due to the change of $n(x)$) and the chemical potential μ , and subsequently changes the flow structure shown in Fig. 2. Using the Thomas-Fermi approximation [22] for a 1D condensate in a harmonic trap, we find that $\mu \propto \omega_x^{2/3}$, and the maximal density $n_{\max} \propto \omega_x^{2/3}$ (i.e. $c_{\max} \propto \omega_x^{1/3}$). By keeping ratios U_s/μ and v_s/c_{\max} fixed, we can construct an equivalent flow structure under a different trapping frequency. We define the scaling factor $\gamma = \omega_x/\omega_x^0$, and incorporate γ into the ratios. This gives rise to the scaling relations, $U_s = \gamma^{2/3}U_s^0$ and $v_s = \gamma^{1/3}v_s^0$. Regime M1 is the modified case for E1, such that $U_s/k = \gamma^{2/3} \times 6$ nK, $v_s = 1.5\gamma^{1/3}v_s^0$; likewise, M2 is the modified case for E2, so $U_s/k = \gamma^{2/3} \times 9$ nK, $v_s = 1.5\gamma^{1/3}v_s^0$.

Our investigation shows that a clear mode structure occurs in regimes where the background flow is sufficiently homogeneous. Then the BdG modes can be described as WKB modes with well-characterized frequency and wavevector, as in Ref. [25]. In the experimental regime (Fig. 3(b) in the paper), ψ_p has the longest wavelength, and is comparable to the width of the BH cavity, L (the distance between the BH and WH horizon). We find that the mode structure is improved when reducing the wavelength of the partner mode ψ_p , relative to L .

To control the wavelength of ψ_p , one can refer to the BCR mechanism and the stimulated Hawking effect, and use the dispersion relation shown in Fig. 10. Overall, the wavelength of the partner mode decreases with increasing step speed, v_s . According to the dispersion relation, the BCR is the zero frequency mode in the WH horizon frame, $\omega(k_{\text{BCR}}) = 0$. Increasing v_s increases the overall speed of the BH cavity, which lowers (raises) the positive- k (negative- k) branch of the dispersion curve $\omega(k)$, and displaces the intersection $\omega(k) = 0$ to larger k (see Fig. 10(a)). This further increases the frequency $|\omega_{\text{HR}}|$ of the Hawking pair, which is proportional to k_{BCR} , and displaces the root of the dispersion curves for ψ_{HR} and ψ_p to larger $|k|$ (see Fig. 10(b-c)). In regime E1, we increase v_s by 50% over the experimental value. This decreases the wavelength of the partner mode relative to the cavity size, L , and the corresponding HR appears more periodic. We further extend L , by increasing step depth, U_s . Regime E2 in Fig. 7 corresponds to the case with a greater step depth, in which the number of oscillations of ψ_p doubles.

Regimes M1 and M2 adopt a smaller trapping frequency, $\omega_x = (1/4)\omega_x^0$. Reducing ω_x increases the size of a BEC, and extends the flow structure, by which excitation modes can be more easily observed and resolved in the laboratory. We can see that cases M1 and M2 maintain a clear mode structure as in E1 and E2, but with approximately twice the cavity size L . Note that regime M2 is reported in the paper, along with a mode analysis using the spatial and temporal WFTs.

A. Growth of the BCR mode in the M2 regime

In the paper, we found that in the experimental regime the standing-wave amplitude n_k inside the cavity (which later proved to be the BCR) grows in proportion to the square of the background density n_{bf} , $n_k \propto n_{\text{bf}}^2$. We use the BCR mechanism to interpret this relationship. If it is indeed the underlying mechanism that occurs in the step-sweeping experiment, the same growth relationship should be found in other parameter regimes.

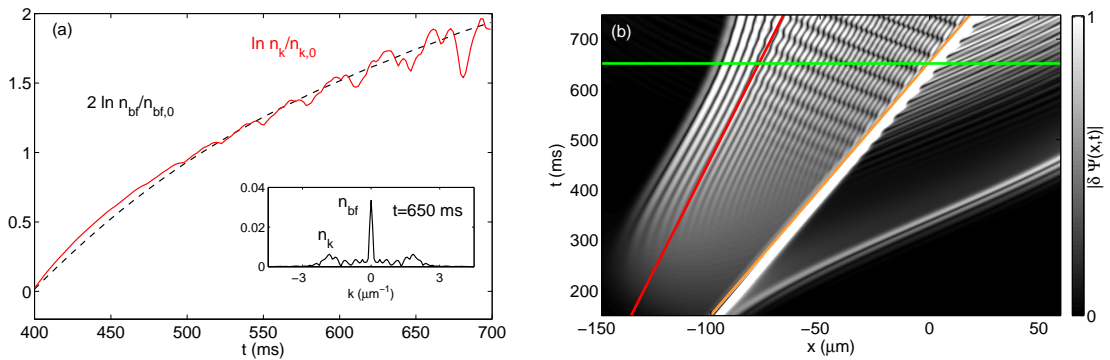


FIG. 8. Growth of the standing wave in the M2 regime. (a) Simulated growth of the standing-wave pattern in the supersonic region. Dashed black: background density $n_{\text{bf}}(t)$; Red: mode growth $n_k(t)$. (b): time evolution of $|\delta\Psi(x,t)|$, from which we select a position nearby the WH horizon, denoted by the red line, to monitor the mode growth. The growth of n_{bf} and n_k is determined from a spatial WFT of $n(x)$ with window width $D = 20 \mu\text{m}$ at the position indicated by the red line in (b). Inset shows the windowed spectrum at $t=650$ ms.

In Fig. 8, we monitor the growth of the standing wave at a position nearby the WH horizon (indicated by the red line in panel (b)). We find that the growth of the standing wave n_k (red curve in (a)) matches that of the background

flow n_{bf}^2 (black curve in (b)), which is consistent with the observation in the experimental regime. For both regimes, the relationship $n_k \propto n_{\text{bf}}^2$ implies that the BCR mechanism along with the increasing background density gives rise to the mode growth inside the cavity, rather than the black-hole lasing effect. Note that the partner mode propagates to the position of observation (the red line in (b)) at late times and causes some small oscillations on the growth plot of n_k .

V. BOGOLIUBOV-DE GENNES MODE ANALYSIS: ASYMPTOTIC MODES, LOCAL DISPERSION RELATIONS, AND THE THERMAL PREDICTION

Here we describe the Bogoliubov-de Gennes (BdG) modes and the relevant calculations discussed in the paper. In V A, we give the standard BdG formalism, and an asymptotic method (WKB) to describe modes on a slowly varying background. In V B, we use the dispersion relation to determine spectral properties of the modes. In V C, we compare the mode amplitudes of the Hawking pair with the thermal prediction using the flow profile at the BH horizon.

A. BdG equations and asymptotic BdG modes

Here we summarize the BdG formulation presented in [22, 25]. The BdG equations can be obtained by the linearization of the condensate wavefunction:

$$\Psi(x, t) = \Psi_0(x, t) + \psi(x, t) \quad (21)$$

where $\Psi_0(x, t)$ corresponds to a stationary condensate, $\Psi_0(x, t) = \sqrt{n(x)}e^{-i\mu t}$, and $\psi(x, t)$ corresponds to a deviation to the background condensate, which can be expressed as

$$\psi(x, t) = e^{-i\mu t} (u(x)e^{-i\omega t} + v^*(x)e^{i\omega t}), \quad (22)$$

where $u(x)$ and $v^*(x)$ satisfy the BdG equations:

$$\begin{aligned} \left[\hbar\omega + \frac{\hbar^2}{2m} \frac{d^2}{dx^2} - V(x) - 2gn(x) + \mu \right] u(x) &= gn(x)v(x) \\ \left[-\hbar\omega + \frac{\hbar^2}{2m} \frac{d^2}{dx^2} - V(x) - 2gn(x) + \mu \right] v(x) &= gn(x)u(x). \end{aligned} \quad (23)$$

For a homogeneous system, BdG modes can be expressed as plane waves

$$u(x) = u_k \frac{e^{ikx}}{\sqrt{2\pi}}, \quad v(x) = v_k \frac{e^{ikx}}{\sqrt{2\pi}}, \quad (24)$$

where the normalized mode amplitudes u_k and v_k are

$$u_k = \frac{1}{\sqrt{1 - D_k^2}}, \quad v_k = \frac{D_k}{\sqrt{1 - D_k^2}}, \quad (25)$$

where D_k gives the ratio between v_k and u_k , and is determined by the speed of sound $c = \sqrt{gn/m}$,

$$D_k = \frac{1}{mc^2} \left[\sqrt{\hbar^2 c^2 k^2 + \left(\frac{\hbar^2 k^2}{2m} \right)^2} - \frac{\hbar^2 k^2}{2m} - mc^2 \right]. \quad (26)$$

This leads to the dispersion relation

$$\omega(k)^2 = c^2 k^2 + \frac{\hbar^2 k^4}{4m^2}. \quad (27)$$

Using Eq. 27, the BdG modes in the wavevector (k) representation can be converted to the frequency (ω) representation, such that $u_\omega = u_k / \sqrt{d\omega/dk}$ and $v_\omega = v_k / \sqrt{d\omega/dk}$.

Suppose the background condensate is inhomogeneous but varies smoothly in space, the BdG modes can be approximated by the WKB method as described in [25]. The WKB-BdG modes in the ω -representation are

$$\begin{aligned} u_\omega(x) &= \sqrt{\frac{\partial k_\omega(x)}{\partial \omega}} \frac{1}{\sqrt{1 - D_{k_\omega(x)}^2}} \frac{e^{i \int^x k_\omega(x') dx'}}{\sqrt{2\pi}}, \\ v_\omega(x) &= \sqrt{\frac{\partial k_\omega(x)}{\partial \omega}} \frac{D_{k_\omega(x)}}{\sqrt{1 - D_{k_\omega(x)}^2}} \frac{e^{i \int^x k_\omega(x') dx'}}{\sqrt{2\pi}}, \end{aligned} \quad (28)$$

where $k_\omega(x)$ is determined by the local dispersion relation using the local sound speed $c(x)$

$$\omega^2 = c(x)^2 k^2 + \frac{\hbar^2 k^4}{4m^2}. \quad (29)$$

B. Dispersion relations for the BCR mechanism and stimulated pair production

Here we use the local dispersion relations to determine the wavevectors and frequencies of the three BdG modes: ψ_{BCR} , ψ_{HR} , and ψ_{p} . First, we transform the local dispersion relation in the comoving frame of the condensate (Eq. 29, denoted by $\omega_{\text{cm}}(k)$) to an observer frame in which the condensate has nonzero flow velocity

$$\omega = \sqrt{c(x)^2 k^2 + \frac{\hbar^2 k^4}{4m^2}} + v_o(x)k, \quad (30)$$

where $v_o(x)$ is the local velocity of the condensate with respect to the “observer” frame in which the frequency is defined. Then we select two points of observation: x_I inside the BH cavity, and x_O outside. Note that here we use ω and k to indicate the relative frequency $\Delta\omega$ and wavevector Δk adopted in the paper. The local speed of sound and the flow velocity can be evaluated by the wavevector spectrum of $\Psi(x)$ as in Fig. 2(c), in which the dominant peak location gives the wavevector of background flow in the lab frame $k_{\text{bf}}(x)$, and its peak value gives the local density $n_{\text{bf}}(x) = |\Psi(k_{\text{bf}}, x)|^2$. The flow velocity in the BH horizon frame is $v_{\text{BH}}(x) = \hbar k_{\text{bf}}(x)/m - v_s$. The WH horizon is defined by the point where $v(x) + c(x) = 0$, and moves at a speed close to that of $x_L(t)$, the left edge of $|\delta\Psi(x, t)|$ shown in Fig. 9. To estimate the flow velocity in the WH frame, we measure the speed of $x_L(t)$ (denoted by v_L), as shown in Fig. 9. The flow velocity in the WH frame is given by $v_{\text{WH}}(x) = \hbar k_{\text{bf}}(x)/m - v_L$.

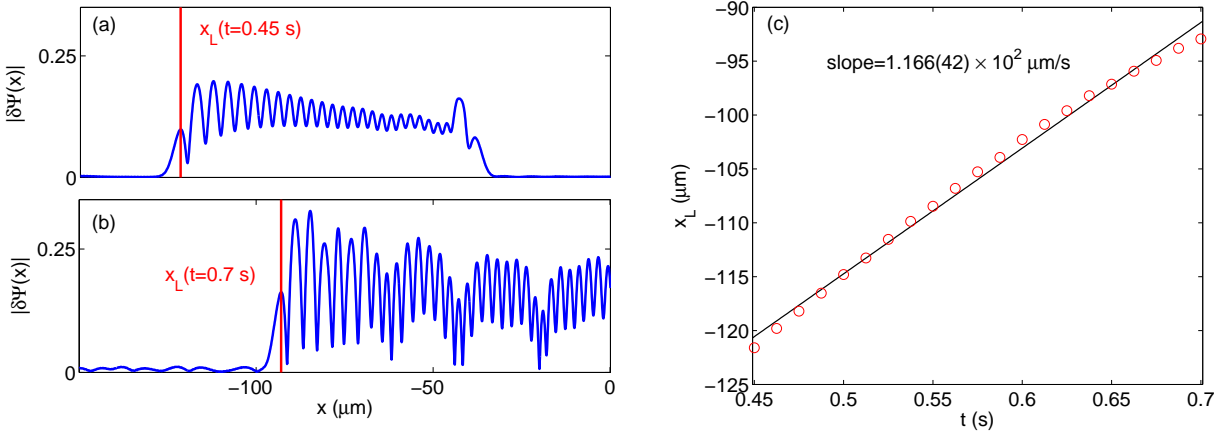


FIG. 9. Determination of the WH velocity. The left edge of $|\delta\Psi(x)|$, x_L , is measured at various times, as indicated by the red lines in (a-b), and the red circles in (c). The speed of the left edge, v_L , is determined by a linear fit on $x_L(t)$, as indicated by the black line in (c), $v_L \sim 0.117$ mm/s.

According to the BCR mechanism, the BCR mode has zero frequency in the WH frame, $\omega(k_{\text{BCR}}) = 0$. We can predict the value of k_{BCR} by the local dispersion relation at x_I using $c(x_I)$ and $v_{\text{WH}}(x_I)$, as shown in Fig. 10(a). This further determines the frequency of the stimulated pair production (see Fig. 10(b-c)); the HR and p modes have the same frequency as that of the BCR mode in the BH frame, given by $\omega = \pm(v_{\text{BH}} - v_{\text{WH}})k_{\text{BCR}} = \pm(v_L - v_s)k_{\text{BCR}}$. This frequency intersects the dispersion relation evaluated at x_I to determine k_p , and the one evaluated at x_O to determine k_{HR} , as indicated in Fig. 10(b-c).

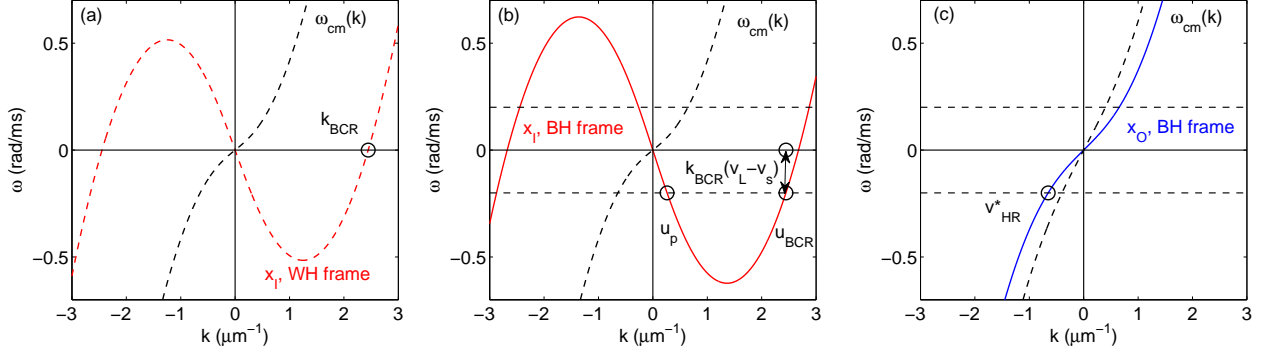


FIG. 10. Dispersion relations. (a) dashed red: the dispersion relation calculated at x_I in the WH frame; (b) solid red: the dispersion relation calculated at x_I in the BH frame; (c) solid blue: the dispersion relation calculated at x_O in the BH frame. Dashed black curve: dispersion relations in the comoving frame of the condensate. The BCR is the zero-frequency mode in the WH frame (a), from which its wavevector k_{BCR} is determined. Transforming the BCR to the BH frames gives rise to the frequency of the HR and partner modes (indicated by horizontal lines) as shown in (b-c).

C. Stimulated pair creation with the thermal prediction

The Hawking temperature can be estimated by measuring the amplitudes of the correlated HR and partner mode. The mode mixing process at the BH horizon is expressed by

$$u_{-\omega}^{\text{BCR}} = \alpha_{-\omega}^{\text{P}} u_{-\omega}^{\text{P}} + \beta_{\omega}^{\text{HR}} (v_{\omega}^{\text{HR}})^*, \quad (31)$$

where $\alpha_{-\omega}^{\text{P}}$ and $\beta_{\omega}^{\text{HR}}$ are the positive-norm and negative-norm amplitudes of the Hawking pair, and $u_{-\omega}^{\text{BCR}}$ and $u_{-\omega}^{\text{P}}$ are the u component of the BCR and the partner mode, $(v_{\omega}^{\text{HR}})^*$ the v component of the HR mode. The ratio of the amplitudes can be calculated using the thermal prediction [6, 10]

$$\left| \frac{\beta_{\omega}^{\text{HR}}}{\alpha_{-\omega}^{\text{P}}} \right|^2 = e^{-\frac{2\pi\omega}{\kappa}}, \quad (32)$$

where κ is the surface gravity at the BH horizon determining the Hawking temperature $T_{\text{H}} = \hbar\kappa/(2\pi k)$,

$$\kappa = \left. \frac{d(v+c)}{dx} \right|_{x_{\text{BH}}}. \quad (33)$$

In Fig. 3(c) in the paper, we trace a correlated Hawking pair (indicated by the magenta and cyan dots) generated at $t = 588$ ms. Using the spatial WFTs, we obtain the mode amplitudes of the pair, $v_{\omega, \text{FT}}^{\text{HR}*}$ and $u_{-\omega, \text{FT}}^{\text{P}}$. Using Eqs. 28-29, they can be expressed in relation to $|\beta_{\omega}^{\text{HR}}/\alpha_{-\omega}^{\text{P}}|$ as

$$\left| \frac{v_{\omega, \text{FT}}^{\text{HR}*}}{u_{-\omega, \text{FT}}^{\text{P}}} \right|^2 = \left| \frac{\beta_{\omega}^{\text{HR}}}{\alpha_{-\omega}^{\text{P}}} \right|^2 \left(1 - D_{k_{\text{p}}}^2 \right) \left(\frac{D_{k_{\text{HR}}}^2}{1 - D_{k_{\text{HR}}}^2} \right) \left| \frac{\partial\omega/\partial k|_{k_{\text{p}}}}{\partial\omega/\partial k|_{k_{\text{HR}}}} \right|. \quad (34)$$

where $D_{k_{\text{HR}}}$ (and $D_{k_{\text{p}}}$) can be evaluated using Eq. 26, and $\partial\omega/\partial k|_{k=k_{\text{HR}}}$ estimated using the dispersion relation.

TABLE II. Numerical values of the relative mode amplitude and the relevant quantities in Eq. 34.

Quantity	Value
$ v_{\omega, \text{FT}}^{\text{HR}*}/u_{-\omega, \text{FT}}^{\text{P}} $	0.11
$ D_{\text{p}} $	0.47 (BdG) 0.40 (FT)
$ D_{\text{HR}} $	0.39 (BdG) 0.44 (FT)
$\partial\omega/\partial k _{k_{\text{p}}}$	-744 $\mu\text{m/ms}$
$\partial\omega/\partial k _{k_{\text{HR}}}$	409 $\mu\text{m/ms}$
$ \beta_{\omega}^{\text{HR}}/\alpha_{-\omega}^{\text{P}} $	0.21

Fig. 11(a) shows the windowed wavevector spectra of a correlated Hawking pair at $t = 650$ ms. The numerical values of the relevant quantities in Eq. 34 are given in Table II. The ratio $|\beta_{\omega}^{\text{HR}}/\alpha_{-\omega}^{\text{P}}| \sim 0.21$. To estimate how well the

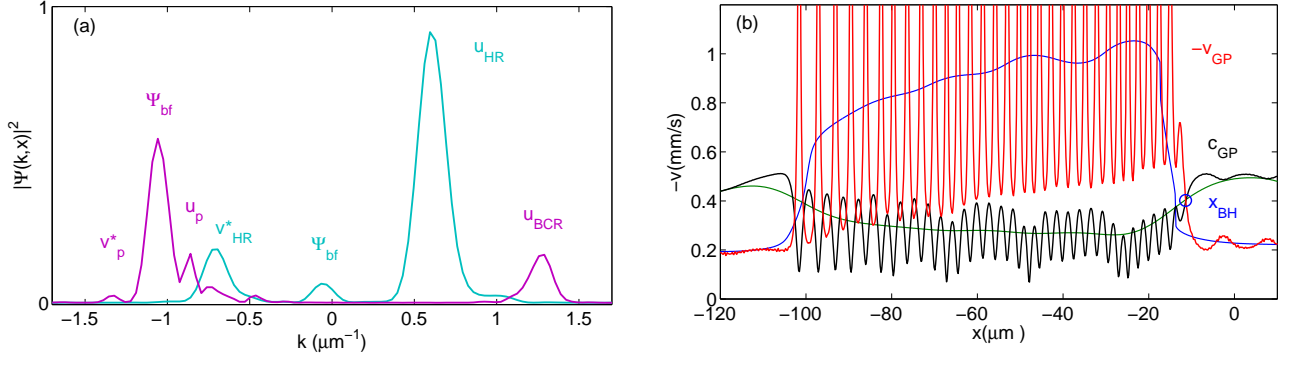


FIG. 11. Spatial WFT for a correlated Hawking pair, and surface gravity near the event horizon. (a) windowed wavevector spectrum of the correlated HR (cyan curve) and partner modes (magenta) at $t = 650$ ms. (b) flow velocity $v_{GP}(x)$ and speed of sound $c_{GP}(x)$ at the time at which the pair is created ($t = 588$ ms). The BH horizon is indicated by the blue circle, x_{BH} . The flow velocity (blue curve) and the speed of sound (green) calculated from the spatial WFT are plotted for comparison. The surface gravity κ is calculated from the speed slopes at the BH.

linear (BdG) approximation works, we measure the quantities $|D_p|$ and $|D_{HR}|$ from the wavevector spectrum (denoted by “FT” in Table II), which correspond to the ratio between the u and v amplitudes of each mode, as indicated in Eq. 28. They differ from the calculated (BdG) values by 13 % for the HR mode, and 15 % for the partner mode.

We also calculate $|\beta_{\omega}^{HR}/\alpha_{-\omega}^p|$ using the thermal prediction (Eq. 32) and the surface gravity κ from (Eq. 33). From the data in Fig. 11(b), we calculate $\kappa = 350 \text{ s}^{-1}$. This corresponds to a Hawking temperature of $T_H = 0.43 \text{ nK}$. The ratio $|\beta_{\omega}^{HR}/\alpha_{-\omega}^p| \sim 0.17$, as determined by the thermal prediction, differs from the value from the WFT (~ 0.21) by 24%.